SUPPLEMENTARY MATERIAL AND EXTENDED DATA FOR:

Structural mechanism of proton pumping by *ba*$_3$-type cytochrome *c* oxidase

Jonatan Johannesson, Doris Zorić, Adams Vallejos, Arpitha Kabbinale, Emil Sandelin, Swagatha Ghosh, Aaron D. Finke, Monika Bjelčić, John Rönnholm, Lucija Ostojić, Johan Glerup, Peter Dahl, Emma Victoria Beale, Claudio Cirelli, Florian Dworkowski, Camila Bacellar, Philip J. M. Johnson, Dmitry Ozerov, Alexander Batyuk, Sebastien Boutet, Gregory M. Gate, Christopher Kupitz, Ariana N. Peck, Frédéric Poitevin, Raymond Sierra, Stella Lisova, Carl Johan Wallentin, Gisela Brändén, Richard Neutze

This document contains:

- Supplementary Methods
- Supplementary Discussion
- Extended Data Figures 1 to 5
- Extended Data Tables 1 to 3
- Captions to Supplementary Videos 1 to 3.
- Supplementary References (47 to 67).

SUPPLEMENTARY METHODS

Purification and crystallization

Protein was produced, purified and crystallized as previously described.[23] Crystallization setups used a well-based technique, which scale favourably when large quantities of *ba$_3$*-type C*c*O microcrystals are required.[47] Purified protein was concentrated to 12 to 15 mg/mL in 20 mM Tris–HCl pH 7.6, 0.05% (*w/v*) DDM, 80 mM NaCl. The protein concentration was determined by reducing the enzyme with excess sodium dithionite, measuring the absorbance at 560 nm and 590 nm, and using the relationship that the absorbance difference $\Delta\varepsilon_{560-590}$ = 26,000 $M^{-1}cm^{-1}$.[48] Concentrated protein was mixed with monoolein [9.9 monoacylglycerol (MAG), Nu-Check Prep; CAS 111-03-5] at a ratio of 2:3 protein to lipid (40 µL of protein and 60 µL of monoolein) using an LCP coupler connected to two gas-tight 100 µL syringes (Hamilton).[49] 10 µL to 15 µL strings of LCP reconstituted protein were dispensed into nine-well glass plates containing 300 µL of 1.4 M NaCl, 100 mM MES pH 5.3 with 36 % to 39 % (*v/v*) PEG 400 and plates were covered with a transparent seal and stored at 20 °C (Molecular Dimensions, ClearVue TM Sheets, MD6-O1S, Lot No: 11024). Microcrystals between 5 µm and 30 µm in their longest dimension were obtained within 2 to 3 days of incubation. Batches containing microcrystals from 15 µm to 25 µm in size were chosen for TR-SFX studies and were transported to SwissFEL and the LCLS in 500 µL syringes (Hamilton).

Photocage degradation

Time-resolved SFX studies at XFEL facilities utilized photocage dioxygen, which could be released using a UV laser pulse.[18,50] Commonly used reducing agents such as sodium dithionite or ascorbate (with a mediator) proved problematic since, in addition to reducing C*c*O, they also degraded the photocage within a few tens of seconds. This time-scale is incompatible with the experimental design since microcrystalline samples must be mixed with photocage in an oxygen tight reservoir for a period of up to two hours prior to delivery across an XFEL beam. A search for alternative reducing agents yielded DTT and DTBA,[51] which slowly reduced C*c*O at pH 5.3 while remaining compatible with the photocage. Using these reducing agents under experimental conditions, the measured half-life of the photocage was 12 hours.

Oxygen scrub

Residual oxygen within microcrystalline slurries will oxidize reduced C*c*O. To minimize the oxygen content of our samples we introduced an oxygen scavenger consisting of glucose oxidase from *Aspergillus niger*, catalase and glucose. By stepwise reducing dioxygen to water, these enzymes shift the chemical equilibrium within samples to achieve a higher overall population of reduced C*c*O. Trade-offs, however, were required since the rate of dioxygen consumption by the oxygen scrub had to be slow relative to the release of dioxygen when using a UV laser pulse. In practice an optimized balance was used throughout these studies consisting of: 2.2 to 2.4 mM of photocage, 170 mM of DTT or 17 mM DTBA, 25 mM Glucose, 0.25 µM glucose oxidase, and 0.15 µM of catalase. Despite these precautions, oxygen could not be completely eliminated from LCP microcrystalline slurries.

Onsite sample preparation

Solid glucose oxidase, catalase and glucose were dissolved in freshly degassed water and further degassed by sparging with nitrogen gas for at least 10 minutes. Monoolein was thawed and melted on a 40 °C heat block and allowed to stand open in a glove box for approximately 16 hours prior to use. A lipidic cubic phase (LCP) was prepared by mixing a 6:4 ratio of monoolein/oxygen scavenger solution mixed between two Hamilton syringes connected with a union, until a clear phase was obtained.

Dithiothreitol (DTT) from a recently purchased unopened bottle, was dissolved in degassed water inside a glove box. DTT solution (40 µl) was added to monoolein (60 µl) and mixed until a homogenous phase was obtained to create the DTT-LCP. Preparations using dithiobutylamine (DTBA) followed the same protocol, except that DTBA was dissolved in 3M NaOH. Solid photocage was dissolved inside a glove box in freshly degassed water and immediately used to prepare the LCP. The LCP was prepared by taking 60 µl of monoolein and mixing it with 40 µl of the caged-O_2 solution to form a black/dark brown caged-O_2-LCP. These steps were carried out in the dark to protect the photocage from exposure to light, including the use of aluminium foil to fully surround samples.

Microcrystals grown in the home laboratory were packed in 500 µl air-tight Hamilton syringes and transported to XFEL user facilities at the Paul Scherrer Institute in Switzerland (SwissFEL) and to SLAC in Stanford, USA (LCLS). These samples were divided into two syringes with a union, the oxygen scavenger LCP was added as 10 % by volume, and mixed until a homogenous phase was obtained. This mixture was allowed to rest for at least one hour prior to treatment with the reductant. Oxygen scrubbed microcrystal preparations were then reduced by the addition of the DTT-LCP or DTBA-LCP (10 % by volume) and given at least one hour to reduce microcrystals before any further steps were taken. DTT or DTBA reduced *ba*$_3$-type C*c*O microcrystal aliquots (80 µl) were then divided between two Hamilton syringes, and caged-O_2 LCP (20 µl) was added and mixed, to obtain a dark black/brown LCP which was ready to be loaded into a 120 µl high-viscosity injector.[22] Samples were protected from exposure to light throughout these steps.

Samples were loaded into an air-tight high-viscosity injector[22] in an anaerobic chamber (glove box) and sealed in an air-tight heat-sealed plastic bag for transport to the beamline. 5 µl to10 µl of a protective oxygen scavenger LCP plug was added at both ends of the sample within the reservoir, which created a protective barrier against oxygen gas diffusion during sample handling and mounting outside of the glove box. The airtight bag was opened immediately prior to data-collection, a 75 µm diameter nozzle tip was inserted, the assembled injector was mounted in the sample chamber, and the sample chamber was filled with low-pressure helium. The final concentrations of all components in the samples used for TR-SFX data collection are: C*c*O (70 µM averaged over the volume of the microcrystalline slurry), glucose (25 mM), glucose oxidase (0.2 µM), catalase (0.15 µM), Caged-O_2 (2.4 mM) and DTT (170 mM) or DTBA (17 mM). For comparison, the concentration of C*c*O in LCP crystals is 2.9 mM. Theoretical models suggest that it would take the order of 1 ms for O_2 to diffuse into microcrystals 10 µm in the smallest dimension.[17,52]

In house time-resolved spectroscopy

A sequence of absorption spectroscopy measurements was recorded using a standard in-house spectrophotometer to follow the reduction of detergent solubilized ba_3-type C*c*O (5 µM concentration) using 2 mM reducing agent. Samples were purged of oxygen, sealed in an oxygen tight cuvette and mixed with DTBA or DTT. These absorption spectra were decomposed to extract the time-dependent populations of the oxidized state and the reduced states of both haem *b* and haem a_3 (**Extended Data Fig. 1**). Basis-spectra for haem *b* and haem a_3 were reconstructed as linear sums of the first three singular value decomposition (SVD) components of these time-dependent data and imposing the condition that the positive feature at 560 nm is unique to the reduced form of haem *b*.

Time-resolved spectroscopy measurements utilized a microspectrophotometer modified from an earlier design,[53] and samples were passed through an air-tight capillary[54] onto which a solid-state ns laser pulse with $\lambda = 355$ nm was focused. Samples of detergent solubilized *ba*$_3$-C*c*O were treated with DTT and mixed with photocage, and spectra were recorded for the time-delays: $\Delta t = 2$ µs, 10 µs, 50 µs, 100 µs, 150 µs, 200 µs, 500 µs, 1 ms, 1.5 ms, 2ms and 10 ms following the release of dioxygen using a UV laser flash (**Extended Data Fig. 2a**). Time-resolved difference spectra were decomposed using SVD analysis and the time-evolution of the principal component was extracted (**Extended Data Fig. 2**, **b** and **c**). Similar measurements were performed on microcrystalline slurries for the time-delay $\Delta t = 1$ ms (**Extended Data Fig. 2d**). All difference spectra shown in **Extended Data Fig. 2** have had the change in the absorption of the photocage following the UV laser pulse removed. Data recorded from microcrystalline slurries also showed two sharp negative absorption features (figure 6 of reference[18]) that were later identified as arising from very low levels of stray light from an energy saving lamp entering the spectrophotometer, and these artefacts were removed.

Onsite spectroscopy

Absorption spectra from microcrystalline slurries were measured from samples held in air-tight Hamilton syringes using a device previously described.[54] A cloudy LCP background often arose from each of the mixing steps described above, and varying levels of contamination were sometimes observed that potentially arose from small quantities of iron dissolved from the Hamilton syringe connectors. For these reasons, no reliable spectra were recovered from microcrystalline slurries during the first experiment at SwissFEL. When later working at the LCLS, this device yielded microcrystal spectra from which it could be determined that DTBA treated samples were almost 100 % reduced (**Extended Data Fig. 1g**).

TR-SFX data-collection

In the first SFX experiment at the Alvra beamline at SwissFEL, SFX diffraction data were collected at 100 Hz from microcrystals of the *ba*$_3$-C*c*O in their resting (oxidized) state, after DTT treatment, and after DTT treatment with photocage added. Mounted samples were extruded downwards into the focused XFEL beam (FWHM of 6 × 6 μm^2) through a 75 μm nozzle using an LCP injector.[22] The X-ray energy was 12 keV and XFEL pulses were 70 fs in duration. To prevent the LCP microjet from exploding and thereby maintain a stable LCP microjet, XFEL pulses of 700 μJ were attenuated to 20 % of the maximum fluence at the sample position. X-ray diffraction images were recorded on Jungfrau 4Mpix detector using a pixel size of 75 × 75 μm^2 and read-out at a frame-rate of 100 Hz. Preliminary TR-SFX data-collection strategies were also explored during this experiment. From these data we concluded that the best strategy was to explore the use of a slightly stronger reducing agent so as to improve the crystallographic occupancy of the reacting species

In a follow-up study, TR-SFX data were therefore recorded from DTBA reduced microcrystals at the MFX beamline of the LCLS. DTBA was chosen as it was better able to reduce LCP *ba*$_3$-type C*c*O microcrystals grown at pH 5.3. The LCLS beam was set at 9.5 keV, X-ray pulses were 30 fs in duration and operated at a repetition rate of 30 Hz, which was chosen to match the configuration of the Rayonix X-ray detector. The XFEL beam was focused to a FWHM spot-size of 4 × 4 μm^2. Due to technical failures in advance of beamtime, a sub-optimal laser configuration was utilized to deliver 355 nm UV pulses of 5 ns in duration at 10 Hz. This Opotek Radiant QX20 laser beam could not be focused on the LCP microjet to smaller than 750 × 750 μm^2 FWHM spot size. A pulse energy of 800 uJ was therefore used to give an average fluence through the full width half maximum of the laser spot laser spot of $F = 90$ mJ/cm^2. The ratio $\sigma_{355nm} \cdot F/h \cdot \nu \approx 4$ ($\sigma_{530nm} = 6500$ $M^{-1} \cdot cm^{-1}$ is the absorption cross section of the photocage at 355 nm, h is Planck's constant, ν is the frequency of the incoming light), implying that multiple UV photons may have been absorbed by every caged oxygen compound per laser pulse, which may have helped to overcome the very poor quantum yield of this photocage.[50]

The 30 Hz XFEL exposure sequence was pump laser on ($\Delta t = 3.3$ ms), laser off (dark 1, $\Delta t = 36.7$ ms) and laser off (dark 2, $\Delta t = 70.0$ ms). With an LCP microjet flow rate of 1.5 µl/min, microcrystals translated downwards approximately 440 µm in 70.0 ms on average. A razor blade was placed 175 µm above the X-ray beam to shade the laser spot on the microjet and thereby prevent direct UV exposure of the region of the LCP microjet from which dark 2 data were collected. This data set was used as reference for calculating the $F_{obs}(\Delta t = 3.3 \text{ ms}) - F_{obs}(\text{dark } 2)$ difference Fourier electron density map shown in **Fig. 3a**. Since the same sample was used for both measurements, this establishes that dioxygen released by the UV laser pulse caused and increase in electron density for Wat300 and a decrease in electron density for Wat301. Moreover, there are no obvious artefacts that may be ascribed to laser induced heating.

Synchrotron X-ray diffraction data collection

Anomalous X-ray diffraction data were recorded from a single crystal at the BioMAX instrument of MAX IV Laboratory using a wavelength of 2.0 Å (6.2 keV). Larger crystals were grown in the presence of oxygen as described above, but with the PEG400 concentration raised to 40 %. Crystals were flash-frozen without cryo-protectant and without mixing with reducing agent. CCP4 was used to process single-crystal data and the anomalous diffraction signal (**Fig. 2A**) was extracted by keeping separate measured X-ray diffraction intensities with opposite sign for their Miller indices.

Serial X-ray crystallography studies were also performed at BioMAX of MAX IV Laboratory, and ID29 of the ESRF, using the flow-cell device for sample delivery.[54] Serial synchrotron X-ray crystallography data were recorded from a small set of microcrystalline samples treated with DTT or DTBA (**Extended Data Table 2**), for which an optical absorption spectrum was recorded immediately prior to X-ray diffraction data-collection. These spectra allowed for the average level of reduction of microcrystals to be quantified.

Data processing and structural analysis

Diffraction data were indexed, integrated, merged and converted to MTZ format using CrystFEL versions 0.9.1, 0.10.1 and 0.10.2.[55,56] X-ray diffraction data were indexed, and the geometry was optimized for detector shift and beam position drift, for every independent sample reservoir. Indexing of SFX data collected at SwissFEL was performed by indexamajig using the input cell parameters from pdb entry 5NDC and several indexing programs (xgandalf-latt-cell, asdf-latt-cell, dirax-latt-cell, mosflm-latt-cell). Data scaling and merging was performed using partilator with three iterations and a unity model, with 2/m_uab the chosen point group. The output of merging were .hkl files that were used as input for check_hkl and compare_hkl, from which figures of merit were extracted. A final resolution of 1.7 Å was chosen for the resting oxidized *ba*$_3$-CcO structure, 1.8 Å for the DTT-reduced *ba*$_3$-CcO structure, and 1.9 Å for the DTT-reduced, with the TR-SFX data from SwissFEL being processed to 1.8 to 2.2 Å resolution (**Extended Data Table 1**).

SFX data collected at LCLS were processed in Beamtime with Xrays (BTX), a user environment containing miscellaneous functions to aid analysis such as calibration files, documentation, scripts and other code. Peak finding, indexing, and merging of diffraction data, as well as geometry optimization, were performed via standardized pipeline defined by yaml files. Indexing was performed by programs mosflm and xds, with standard input cell parameters *ba*$_3$-CcO microcrystals. Data scaling and merging were performed in the same manner as used to process data collected at SwissFEL. A final resolution of 2.35 Å was chosen for the fully-reduced *ba*$_3$-*CcO* structure after DTBA treatment (**Extended Data Table 1**) and up to 2.1 Å for TR-SFX data.

Data truncation, phasing and structural refinement were performed in the CCP4i suite (version 9.0.003).[57] Molecular replacement was carried out in Phaser[58] using previously published resting oxidized room-temperature SFX structure of *ba*$_3$-C*c*O (PDB ID: 5NDC). Structural refinement was performed in Refmac5[57] utilizing a pipeline consisting of 20 cycles of maximum likelihood rigid body refinement followed by several rounds of maximum likelihood restrained refinement, including TLS refinement.[57] Electron density maps were inspected and model building was performed in Coot.[59] Final values for R_{work} and R_{free} are given in **Extended Data Table 1**. All structural representations were drawn in PyMOL.[60] For almost all data-sets, structures were modelled with a single structure. Selected water molecules and both active-site Cl^- atoms were modelled with partial occupancy, with their occupancy fixed according to the integrated sum of the Polder omit map electron density (calculated using phenix.polder, Phenix v1.19.2-4158) within a 1 Å radius of their atomic positions.[61] For a subset of data-sets, Ser400$_A$ and Tyr402$_A$ were modelled with two conformations having complementary partial occupancy, and some variation was observed for a small number of surface exposed side-chains.

Extrapolated data

Data extrapolation has been developed to aid the interpretation of electron density for time-dependent species with partial occupancy. For light-initiated reactions, it is assumed that structure factor amplitudes for any time-dependent species can be extrapolated to 100% occupancy by removing the contribution from molecules within crystals that are not activated by the light pulse. This approach has been implemented in the program Xtrapol8 and the method is described in detail.[37] Extrapolated structure factor amplitudes for the delay Δt = 3.3 ms were calculated using the programme Xtrapol8 using microcrystalline slurries treated with DDT and mixed with photocage, but not exposed to UV light, as a reference. Extrapolated electron density maps were generated in Xtrapol8 using all possible options and assuming an extrapolation factor of the time-dependent species of interest ranging from 20% to 100% in 10% increments. The extended Fgenic method described in reference[62] gave an extrapolation factor estimate of 40 % using the difference-map method described in reference.[37] In parallel, the occupancy of the O^4 state in the Δt = 3.3 ms TR-SFX data was estimated by calculating Polder omit maps[63] about the coordinates of Wat300, quantifying these Polder omit map densities using the approach described in references,[61,64] and comparing with the quantified Polder omit map electron density for very well-ordered water molecules elsewhere in the structure. This analysis also suggested 40 % for the occupancy of Wat300, a water molecule that we consider to be unique to the light-activated state. Using the extended Fgenick method in Xtrapol8 with an extrapolation factor of 40 % and refining structural models in phenix.refine (Phenix v1.19.2-4158) against these extrapolated data, yielded *R*-work = 24 % and *R*-free = 27 %. **Figure 3c** shows the resulting $2mF_{extr,40\%}(\Delta t = 3.3\text{ ms}) - DF_{calc}$ electron density map. **Figure 3d** shows the isomorphous $F_{extr,40\%}(\Delta t = 3.3\text{ ms})$ - F_{obs}(DTBA treated) difference Fourier electron density map.

Building water molecules with partial occupancy

To identify transient water molecules, we inspected $2mF_{obs}$ - DF_{calc} electron density maps, mF_{obs} - DF_{calc} Polder omit electron density maps[63] (where m is the figure of merit and D is a sigma weighting factor), isomorphous F_{obs}-F_{obs} difference Fourier electron density maps, [65] and electron density maps calculated using extrapolated data.[37] Wat301 was modelled in all structures treated with DTT and DTBA. Wat300 was modelled only for the time-delay $\Delta t = 3.3$ ms. Additional evidence for weaker, transiently ordering water molecules was observed in Polder omit maps when only a single chloride was modelled in the active-site (**Fig. 3b**) but these residual electron density features were judged to be too weak to model with confidence according to accepted crystallographic criteria.

Numbering of water molecules

Water molecules have been renumbered relative to previously deposited X-ray structures of the *ba*3-type C*c*O in order to make the text easier to follow. Water molecules numbered from 300 to 309 are within the active-site; Water molecules from 310 to 319 are associated with the K-channel analogue on the *N*-side of the active-site; Water molecules from 320 to 329 are associated with the PLS on the P-side of the active-site.

Referring to residue numbers

We follow the convention that all residues referred to in the text or in captions to figures correspond to subunit-I of the *ba*3-type C*c*O unless otherwise specified.

SUPPLEMENTARY DISCUSSION

Structural perturbation of TM10 upon reduction of ba$_3$*-type C*c*O.*

Transmembrane α-helix perturbations have been reported for C*c*Os[17,66,67] but their functional significance is unclear. Evidence for an α-helix perturbation in the *ba*$_3$-type CcO is visible in the isomorphous F_{obs}(DTBA treated) - F_{obs}(oxidised) difference Fourier electron density map, which shows paired negative and positive difference density features associated with residues 399 to 402 on the N-side of TM10 of subunit I (**Extended Data Fig. 4**), reminiscent of a structural change in TM10 of bovine *aa*$_3$-type CcO.[67] In the resting oxidised structure, this region is stabilized by water mediated H-bond interactions including Wat352 and Wat353, which form hydrogen bonds to the backbone carbonyl oxygens and polar side-chains of residues 396 and 403 in TM10, and 345 of TM9. Upon reduction, Wat352 is lost, which disrupts this H-bond network and potentially increases protein flexibility in this region. This may have a modest influence on proton uptake, since the T396V mutation within TM10 slows enzymatic turnover.[6] This structural transition upon reduction of *ba*$_3$-type C*c*O was reproducibly observed, irrespective of whether DTBA (**Extended Data Fig. 4, a** and **c**) or DTT (**Extended Data Fig. 4, b** and **d**) were used to reduce microcrystalline samples. However, the reverse transition was not evident within either of the $F_{obs}(\Delta t = 3.3$ ms) - F_{obs}(dark 2) and $F_{obs}(\Delta t = 3.3$ ms) - F_{obs}(DTBA treated) isomorphous difference Fourier electron density maps. We therefore characterize this structural transition as associated with a slow conformational change to the resting oxidized conformation upon treatment with reducing agent.

Nonlinear nature of Cl^- binding to Cu_B.

To better characterize the binding of Cl^- to *ba*$_3$-type C*c*O, we selected a sub-set of DTT and DTBA treated microcrystalline samples from which both serial X-ray crystallography data-collection and quantitative spectral measurements were recovered. From these data we quantified the electron density associated with both Cl^- ions as a function of the measured level of reduction of microcrystals. Polder omit electron density maps[63] were calculated with both Cl^- ions removed from the model, and their Polder residual electron densities were integrated within a 1.0 Å radius about the coordinates of each Cl^- atom.[61] Integrated Polder electron density values are plotted against the measured level of reduction of ba_3-type microcrystalline slurries in **Extended Data Fig. 3, a** and **b**. These plots reveal that the electron density for the Cl^- ligand to the farnesyl oxygen of haem a_3 decreases linearly as microcrystals are reduced **(Extended Data Fig. 3a)**, whereas the electron density for the Cl^- ligand to Cu_B decreases nonlinearly as microcrystals are reduced **(Extended Data Fig. 3b**). Because electrons exchange between cofactors when the enzyme is only partially reduced, Cl^- ions may dissociate from Cu_B when this metal is reduced to Cu(I), and may rebind to Cu_B when this metal is oxidized to Cu(II) and the electron resides on another cofactor. Moreover, the time required for Cl^- ions to dissociate from Cu(I) and migrate away from the BNC is unknown. These dynamic effects will cause electron density to be visible within the BNC until a high fraction of C*c*O molecules within microcrystals are fully reduced, and this explains the nonlinearity displayed in **Extended Data Fig. 3b**.

Electron density changes within the BNC

Four electrons are required to fully reduce each ba_3-type C*c*O molecule. For TR-SFX experiments we chose DTBA, a relatively weak reducing agent, to reduce the crystallized enzyme since DTBA preserves a lifetime of approximately twelve hours for the photocage in solution,[18] whereas more commonly used reducing agents such as ascorbate or dithionite degrade the photocage within tens of seconds. It took approximately two hours to mix DTBA treated microcrystals with photocage, load them into a reservoir, mount them at the LCLS experimental station and inject these samples across the XFEL beam. Because photocaged oxygen decays slowly when solubilized, it was not possible to entirely remove dioxygen from LCP microcrystal slurries mixed with photocage. Consequently, a fraction of DTBA treated *ba*$_3$-type C*c*O molecules will be oxidized to the O^4-state by residual oxygen. Moreover, because the resting oxidised structure shows Cl$^-$ bound to both Cu$_B$ and to the farnesyl oxygen of haem *a*$_3$ (**Fig. 2a**), Cl$^-$ will eventually bind to the re-oxidized form of *ba*$_3$-type C*c*O but the rate of Cl$^-$ binding is unknown. These (empirically slow) processes will not violate the electroneutrality principle because the charge of the first Cl$^-$ will cancel the charge lost as OH$^-$ is protonated and departs the BNC as H_2O, and the charge of the second Cl$^-$ will be compensated for by the PLS being reprotonated, despite haem *b* remaining oxidized. Excess DTBA will also re-reduce oxidized *ba*$_3$-type C*c*O on a time-scale of several tens of minutes. These complex kinetics explain why the isomorphous F_{obs}(dark 2) - F_{obs}(DTBA treated) difference Fourier electron density map shows positive difference density within the BNC (**Extended Data Fig. 3d**, maximum ~ 9.4 σ) that suggest the presence of both an OH$^-$ ligand binding to haem *a*$_3$ in a fraction of *ba*$_3$-type C*c*O molecules, and a Cl$^-$ ligand binding to Cu$_B$ of *ba*$_3$-type C*c*O in another fraction of molecules. Likewise, the isomorphous $F_{obs}(\Delta t = 3.3$ ms) - F_{obs}(DTBA treated) difference Fourier electron density map shows positive difference electron density within the BNC (**Extended Data Fig. 3c**, maximum ~ 10.5 σ) that also indicates OH$^-$ binding to haem *a*$_3$ in a fraction of *ba*$_3$-type C*c*O molecules, and Cl$^-$ binding to Cu$_B$ in another fraction of *ba*$_3$-type C*c*O molecules. A positive difference electron density feature associated with Wat300 (maximum ~ 4.6 σ) and a negative difference electron density feature associated with Wat301 (minimum ~ -5.4 σ) are also visible in this map.

As with $F_{obs}(\Delta t = 3.3$ ms) - F_{obs}(DTBA treated), the $F_{obs}(\Delta t = 3.3$ ms) - F_{obs}(dark 2) difference Fourier electron density map shows positive difference electron density associated with Wat300 (maximum ~ 4.1 σ) and negative difference electron density associated with Wat301 (minimum ~

-3.6 σ) (**Fig. 3a**). However, a positive difference electron density feature within the BNC that could potentially indicate an increase in the population of OH^- ligating haem *a*3 is too weak (maximum ~ 2.5 σ) to be assigned. Because OH^- is believed to ligate haem *a*3 in the O^4 state (**Supplementary Video 3, Extended Data Table 3**), this lack of difference electron density adjacent to the iron of haem *a*3 at first appears puzzling. However, this may be explained by hypothesizing that the influx of O_2 into the active site following a UV laser pulse displaces some electron density that would otherwise arise from the presence of Cl^- within the BNC. Specifically, **Extended Data Fig. 3e** presents a difference Fourier electron density map calculated from theoretical data in which an O_2 impulse is modelled as inducing a 40 % increase in the occupancy of an oxygen ligand to haem *a*3, a 40 % increase in the occupancy of Wat300, a 40 % decrease in the occupancy of Wat301, and a 10 % decrease in the occupancy of the Cl^- ligand to Cu_B. This theoretical map (noise is added to the modelled structure factor amplitudes) displays the expected positive difference electron density feature associated with Wat300 and the negative difference electron density feature associated with Wat301. However, the anticipated positive difference electron density feature associated with the OH^- ligand to haem *a*3 is much lower in magnitude than the difference electron density features associated with Wat300 and Wat301. This is because the coordinates of the modelled hydroxide ion are closer (~1.2 Å) to the coordinates of the modelled Cl^- ligand of Cu_B than the resolution (2.2 Å) of the theoretical difference Fourier map, and therefore competition between ordering and disordering events within the BNC partially cancel their respective difference electron density contributions. Although the strength of interpretable difference electron density features in difference Fourier maps grows approximately linearly with the change in occupancy, below a critical change in occupancy threshold, the noise inherent in the data dominate and it is not possible to distinguish the feature at all. Our experience suggests that for a difference Fourier map calculated at 2.2 Å resolution from a large membrane protein complex, the minimum change in occupancy of a single oxygen atom would need to be larger than 20 % for the corresponding feature to be visible above 3.0 σ. Thus, even a relatively small change in the effective occupancy of Cl^- (which has 18 electrons, compared with oxygen's 8) within the active site could obscure a positive difference density feature associated with a very close water molecule.

Another viewpoint is provided by calculating the isomorphous $F_{obs}(\Delta t = 3.3\text{ ms}) - F_{obs}(\text{DTBA treated \#2})$ difference Fourier electron density map against serial X-ray crystallography data collected from microcrystalline slurries that were not 100 % reduced upon DTBA treatment (DTBA treated #2). The resulting difference Fourier map (**Extended Data Fig. 3f**) also shows a positive difference electron density feature (maximum +5.4 σ) due to Wat300 ordering in H-bond contact with Tyr237, a second positive difference density feature (maximum +6.5 σ) that indicates an OH^- ligand to the iron atom of haem a_3, and complementary negative difference electron density (minimum -3.8 σ) that suggests that the haem iron is slightly displaced towards the new ligand. As with the $mF_{obs}(\Delta t = 3.3\text{ ms}) - DF_{calc}$ Polder omit difference electron density map (**Fig. 3b**), there is some positive electron density that is visible in the $F_{obs}(\Delta t = 3.3\text{ ms}) - F_{obs}(\text{DTBA treated \#2})$ difference Fourier map that is slightly offset from the coordinates of the Cl^- ligand to Cu_B (**Extended Data Fig. 5f**), and this density could support the hypothesis that a H_2O molecule ligates Cu_B at $\Delta t = 3.3$ ms. There are no significant difference electron density features associated with Wat301 and the Cl^- ligand to Cu_B because the reference dataset (DTBA treated #2) was chosen precisely because it has very similar crystallographic occupancies (within errors) for these atoms as the photoactivated ($\Delta t = 3.3$ ms) dataset.

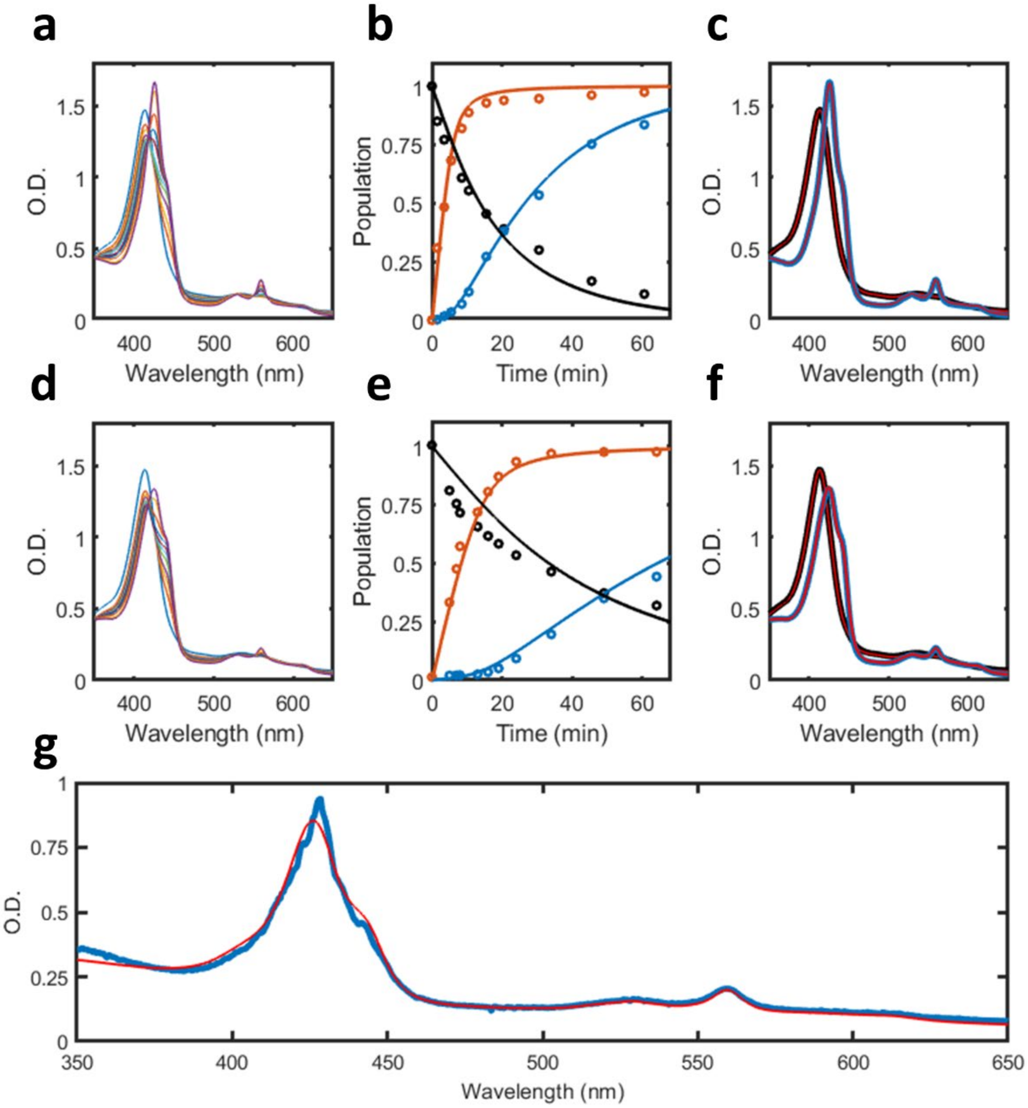

Extended Data Figure 1: Spectroscopic data and analysis during the reduction phase of ba_3 C*c*O. **a**, Time-dependent sequence of UV/vis spectra recorded as detergent solubilized 5 μM ba_3-type C*c*O samples are reduced using 2 mM DTBA. **b**, Decomposition of the time-dependent spectra shown in panel (a) into the population of three sub-components: oxidized (black circles), reduced haem *b* (blue circles) and reduced haem a_3 (red circles). Populations predicted from a kinetics model are shown as solid lines, where the exchange of electrons between cofactors is described by rate-constants optimized to fit these experimental populations. **c**, Initial (black) and final (blue) spectra shown in panel (a) and that predicted by spectral decomposition (red) using the initial and final populations shown in (b). **d**, Time-dependent sequence of UV/vis spectra recorded as detergent solubilized 5 μM *ba*$_3$-type C*c*O samples are reduced using 2 mM DTT. **e**, Decomposition of the time-dependent spectra shown in panel (d) into the population of three sub-components. **f**, Initial (black) and final (blue) spectra shown in panel (d) and that predicted by spectral decomposition (red) using the initial and final populations shown in (e). **g**, Spectrum recorded from DTBA treated microcrystals (blue) immediately prior to data-collection at the LCLS (electron density shown in **Fig. 2c**). Decomposition into oxidized and reduced components (red) indicates that DTBA treated microcrystals were 97 % ± 3 % reduced. Reference spectra used to determine the extent of C*c*O reduction were recorded from detergent solubilized sample as isolated (oxidized) and after treatment with sodium dithionite under oxygen free conditions.

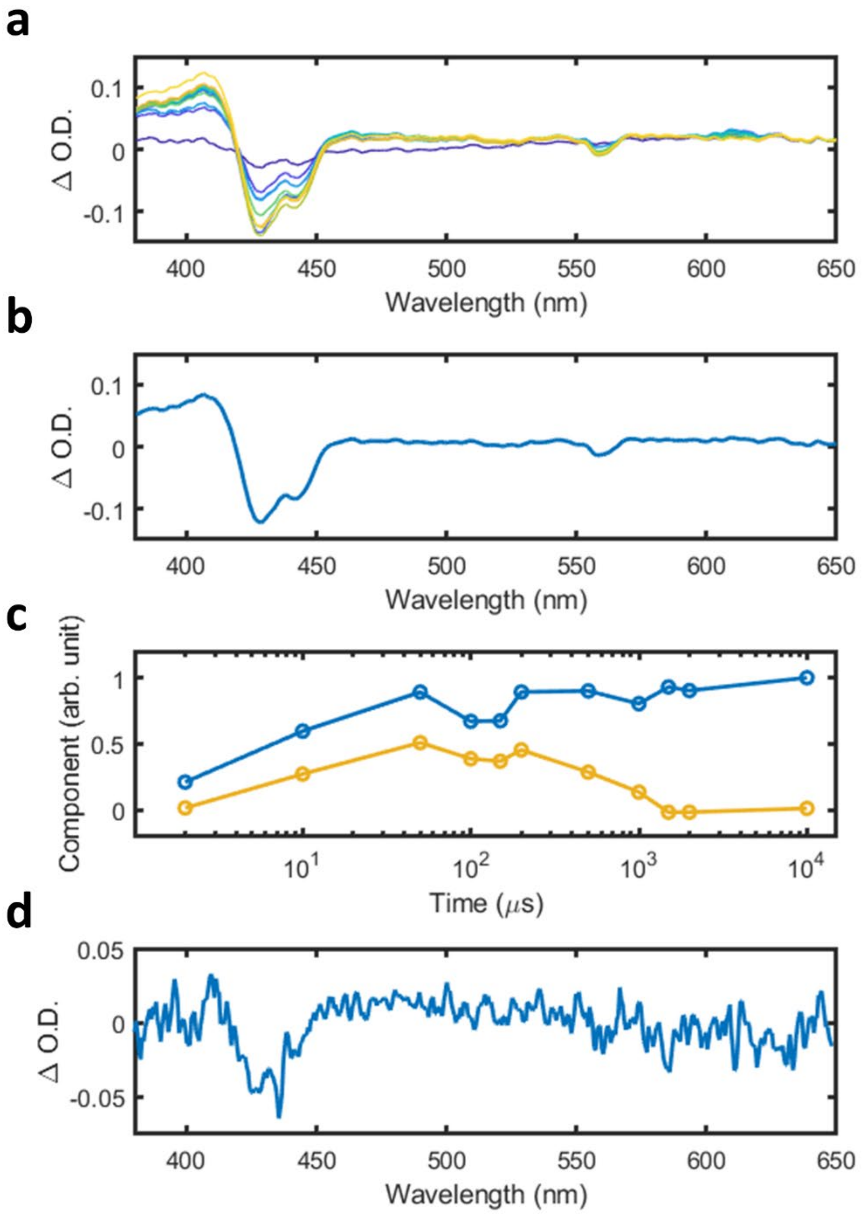

Extended Data Figure 2: Time-resolved spectroscopy study of the oxidation of DTT reduced *ba*$_3$-type C*c*O in solution and in microcrystals as photocage is released by a UV laser pulse. **a**, Time-dependent difference spectra recorded following the release of photocage dioxygen using a ns UV-laser pulse (λ = 355 nm). Data were recorded for the time-delays Δt = 2 µs, 10 µs, 50 µs, 100 µs, 150 µs, 200 µs, 500 µs, 1ms, 1.5 ms, 2.0 ms and 10.0 ms. **b**, Principal SVD component extracted from the data shown in panel (a). This difference spectrum is characteristic of the transition from a reduced to an oxidized state. **c**, Time-dependence of the principal SVD component of the data (blue line and circles). The growth in the population of the principal SVD component is followed by a brief dip for the time-delays Δt = 100 μs and 150 μs, reflecting the transfer of electrons from Cu_A to haem *b*. Time-dependent relative changes in the absorption at 610 nm are also indicated (mustard line and circles) which indicate the growth and decay of the P-state.[45] All observable features and time-scales are consistent with those previously described for time-resolved absorption spectroscopy studies of ba_3-type C*c*O.[35,36] **d**, Time-resolved difference spectra calculated by subtracting spectra recorded from DTT reduced microcrystals mixed with photocage 1 ms after exposure to a UV laser flash, minus spectra recorded from the same microcrystals without any light exposure. These data demonstrate that microcrystals become more oxidized after the UV laser flash. The UV laser induced change in the absorption spectrum of the photocage is removed from panels **a** and **d**, and two non-physical sharp negative absorption features (figure 6 of reference[18]) identified as due to stray light from an energy saving lamp, were also removed.

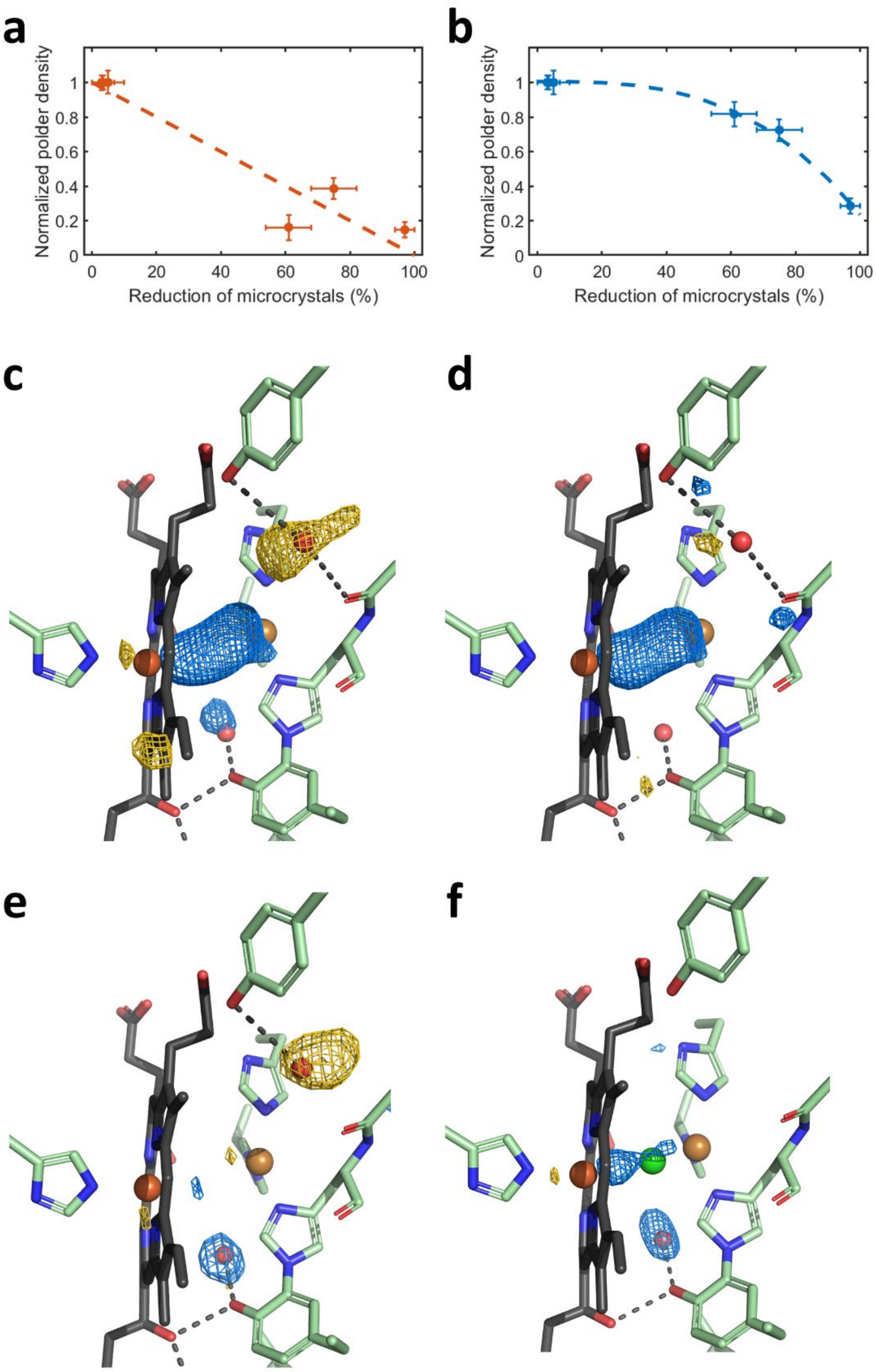

Extended Data Figure 3: Electron density changes within the BNC. **a**, Quantification of mF_{obs} - DF_{calc} Polder omit electron density associated with the Cl^- ion ligating the farnesyl oxygen of haem a_3 as microcrystalline slurries are increasingly reduced. An approximate linear dependence is observed (red dashed line). **b**, Quantification of mF_{obs} - DF_{calc} Polder omit electron density associated with the Cl^- ion ligating Cu_B as microcrystalline slurries are increasingly reduced. A highly non-linear dependence is observed (blue dashed line). Crystallographic data used for these calculations are summarized in Extended Data **Tables 1** and **2**. **c**, Isomorphous $F_{obs}(\Delta t = 3.3$ ms) - F_{obs}(DTBA treated) difference Fourier electron density map (contoured at ± 3.5 σ). **d**, Isomorphous F_{obs}(dark 2) - F_{obs}(DTBA treated) difference Fourier electron density map (contoured at ± 3.5 σ). **e**, Isomorphous F_{calc}(model 1) – F_{calc}(model 2) difference Fourier electron density map calculated from modelled data with added noise. The structural models used to calculate datasets model 1 and model 2 were identical apart from differences in the occupancy of the following selected atoms: Wat300 (40 % higher occupancy in model 1), Wat 301 (40 % lower occupancy in model 1), an OH^- ligand to haem a_3 (40 % higher occupancy in model 1), and the Cl^- ligand to Cu_B (10 % lower occupancy in model 1). Noise was added to these modelled data using random numbers but scaled proportional to $\sqrt{F_{calc}}$, where F_{calc} is the structure factor amplitude calculated from a structural model. **f**, Isomorphous $F_{obs}(\Delta t = 3.3$ ms) - F_{obs}(DTBA treated #2) difference Fourier electron density map (contoured at ± 3.5 σ). The reference data-set DTBA treated #2, was collected from DTBA treated microcrystalline slurries which were not 100 % reduced. Rather, this data set was chosen because the electron density associated with the Cl^- ligand to Cu_B, and the electron density associated with Wat300, matched the corresponding electron density of these atoms recovered from the dataset recorded at $\Delta t = 3.3$ ms.

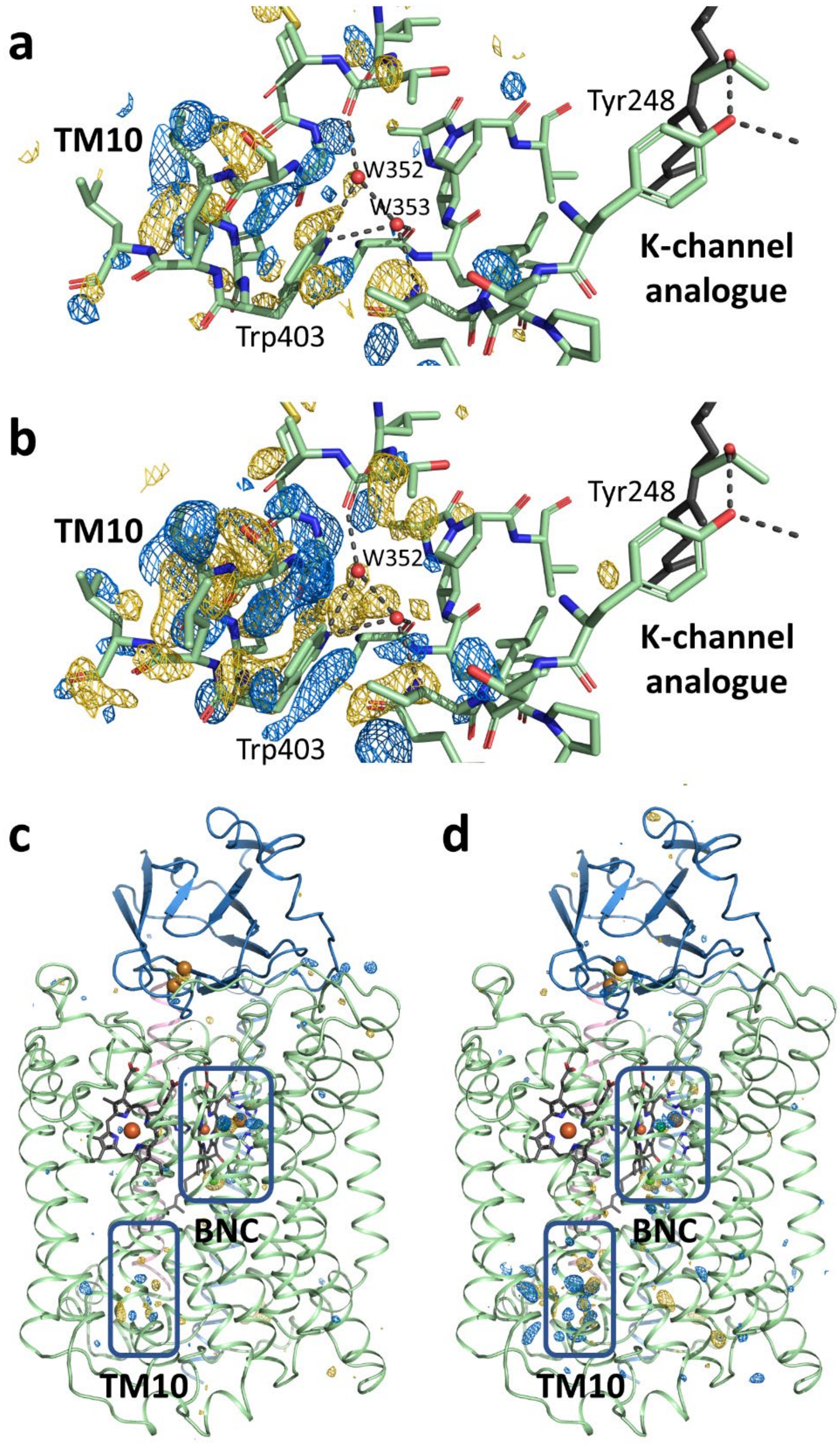

Extended Data Figure 4: Electron density changes in *ba*$_3$-type C*c*O upon treatment with reducing agent. **a,** Isomorphous F$_{obs}$(DTBA) - F$_{obs}$(oxidized) difference Fourier electron density map (blue +3.5 σ; yellow – 3.5 σ) indicating paired difference electron density features associated with the

N-side of TM10. **b,** Isomorphous F_{obs}(DTT + photocage treated) - F_{obs}(oxidized) difference Fourier electron density map (blue +3.5 σ; yellow – 3.5 σ) indicating paired difference electron density features associated with the N-side of TM10. **c**, Long-distance overview of the isomorphous F_{obs}(DTBA) - F_{obs}(oxidized) difference Fourier electron density map shown in panel a and contoured at ± 4.0 σ. **d**, Long-distance overview of the isomorphous F_{obs}(DTBA) - F_{obs}(oxidized) difference Fourier electron density map shown in panel **b** and contoured at ± 4.0 σ.

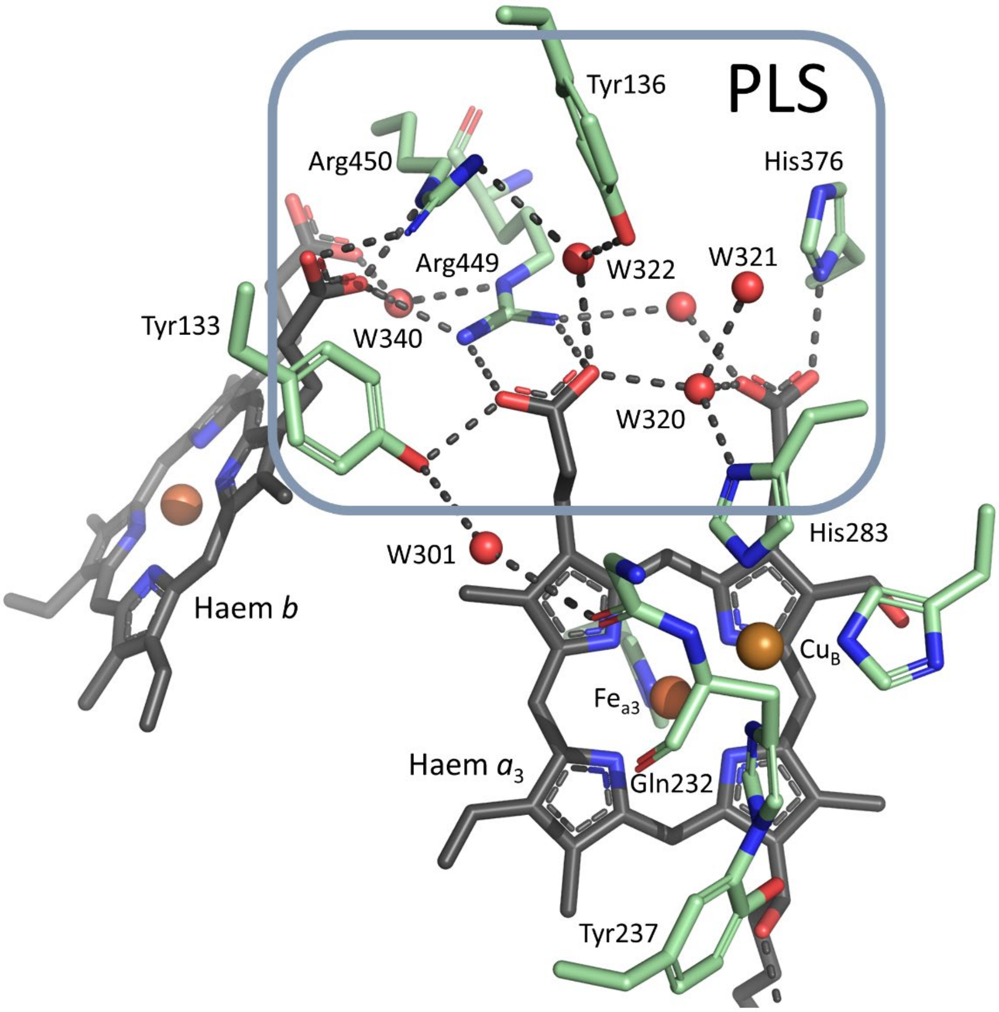

Extended Data Figure 5: Structure of the "proton-loading site" (PLS)[4,5] of the *ba*3-type C*c*O, which accepts protons from the *N*-side and releases protons to the *P*-side as the enzyme turns over. The PLS is formed by the two propionates of haem *a3*, their associated structural water molecules and neighbouring charged or polar residues including Tyr136, Arg449, Arg450 and His367.

Extended Data Table 1: Table of serial crystallography data collected using XFEL radiation

Where collected	**SwissFEL**	**SwissFEL**	**LCLS**	**LCLS**	**LCLS**	**LCLS**
Preparation	Oxidized	DTT + cage treated	DTBA treated	3.3 ms (Light)	36.7 ms (Dark 1)	70.0 ms (Dark2)
PDB code	29OW	29OY	29PD	29OZ	29PB	29PC
Data Collection						
Temperature (K)	293	293	293	293	293	293
Space Group	C121	C121	C121	C121	C121	C121
Cell dimensions						
a, b, c (Å)	145.85, 100.32, 96.62	145.85, 100.32, 96.62	145.85, 100.32, 96.62	145.85, 100.32, 96.62	145.85, 100.32, 96.62	145.85, 100.32, 96.62
α, β, γ (°)	90.0, 126.8, 90.0	90.0, 126.8, 90.0	90.0, 126.8, 90.0	90.0, 126.8, 90.0	90.0, 126.8, 90.0	90.0, 126.8, 90.0
Resolution (Å)‡	1.70-16.5 (1.70-1.74)	1.90-16.7 (1.90-1.95)	2.35-16.7 (2.35-2.41)	2.10-27.5 (2.10-2.16)	2.13-23.1 (2.13-2.17)	2.16-34.7 (2.16-2.20)
R_{split} (%)‡	22.1 (91.5)	17.2 (99.1)	30.8 (117.9)	16.1 (70.1)	15.9 (59.2)	16.3 (53.0)
I/σ(I)‡	4.18 (1.06)	4.17(0.92)	2.6 (0.95)	4.14 (0.84)	4.56 (1.13)	4.52 (1.12)
CC($^1/_2$)‡	0.93 (0.36)	0.96(0.34)	0.88 (0.31)	0.95 (0.56)	0.96 (0.65)	0.95 (0.70)
Completeness (%)	100	100	100	100	100	100
Multiplicity‡	93.1	89.2	58.68	349.5	355.7	372.1
Indexed patterns	29 951	40 076	14 695	65 079	67 206	68 492
Unique reflections	122 041	87 558	46 353	65 027	62 301	59 619
Refinement						
Resolution	1.70-16.54	1.90-16.70	2.35-16.70	2.10-27.50	2.13-23.10	2.16 – 23.1
R_{work}/R_{free} (%)	16.2/18.0	15.9/18.1	18.3/22.2	16.1/19.3	15.4/18.7	15.7/18.9
Number of atoms	6470	6439	6390	6426	6444	6436
Average B factor (Å^2)	33.79	42.44	39.82	43.73	42.11	42.26
R.m.s deviations						
Bond lengths (Å)	0.013	0.011	0.010	0.010	0.011	0.010
Bond angles (°)	1.92	1.73	1.71	1.69	1.71	1.64

‡Values in parenthesis indicate highest resolution shell

Extended Data Table 2: Table of single-crystal and serial crystallography data collected using synchrotron radiation

Where collected	**MAXIV**	**MAXIV**	**MAXIV**	**ESRF**	**ESRF**
Preparation	Oxidized (Anomalous)	Oxidized	DTT treated CcO	DTBA treated CcO	Oxidized CcO
PDB code	9GDF	8HUA	---	---	---
Data Collection					
Temperature (K)	100	293	293	293	293
Space Group	C121	C121	C121	C121	C121
Cell dimensions					
a, b, c (Å)	143.7, 98.3, 94.1	146.1, 100.2, 96.6	145.9, 100.3, 96.6	145.9, 100.3, 96.6	145.9, 100.3, 96.6
α, β, γ (°)	90.0, 127.6, 90.0	90.0, 126.8, 90.0	90.0, 126.8, 90.0	90.0, 126.8, 90.0	90.0, 126.8, 90.0
Resolution (Å)‡	2.28-74.5 (2.32 – 2.28)	2.12-25.4 (2.20–2.12)	2.30-69.6 (2.30-2.28)	2.31-32.5 (2.31-2.35)	2.45-32.5 (2.45-2.49)
R_{split} (%)‡	--	10.4 (78.1)	17.5 (50.3)	8.9 (102.9)	12.0 (95.5)
Rmerge‡ (all I+ & I-)(%)	17.9 (84.2)	--	--	--	--
Rmeas‡ (all I+ & I-)(%)	18.2 (89.2)	--	--	--	--
Rpim‡ (all I+ & I-)(%)	3.2 (28.1)	--	--	--	--
I/σ(I)‡	18.0 (2.3)	7.0 (1.2)	4.7 (1.9)	8.1 (1.1)	6.32 (1.1)
CC($^1/_2$)‡	99.8 (72.7)	99.1 (55.9)	96.7 (76.3)	99.0 (29.0)	98.0 (30.0)
Completeness‡ (%)	94.4 (63.3)	100 (100)	100 (100)	100 (100)	100 (100)
Multiplicity‡	29.2 (9.2)	124.8 (82.7)	318.7 (234.3)	510.6 (337.5)	272.25 (194.12)
Unique reflections	44 643	63 185	97 509	48 976	41 044
Refinement					
Resolution	2.28-74.5	2.12-25.8	2.30-69.6	2.31-32.5	2.45-32.5
R_{work} / R_{free} (%)	15.31/19.65	16.1/18.8	15.28/19.43	15.40/19.93	15.72/20.79
Number of atoms	6402	6380	6429	6409	6388
Average B factor (Å^2)	47.693	52.00	50.48	53.88	58.78
R.m.s deviations					
Bond lengths (Å)	0.009	0.013	0.010	0.010	0.010
Bond angles (°)	1.70	1.84	1.75	1.77	1.89
Anomalous					
Anomalous completeness	93.6				
Anomalous multiplicity	14.9				
CC(ano)	0.443				
|DANO|/sd(DANO)	0.776				

‡Values in parenthesis indicate highest resolution shell

Extended Data Table 3: Mechanism of proton pumping by *ba*$_3$-type *C*cO

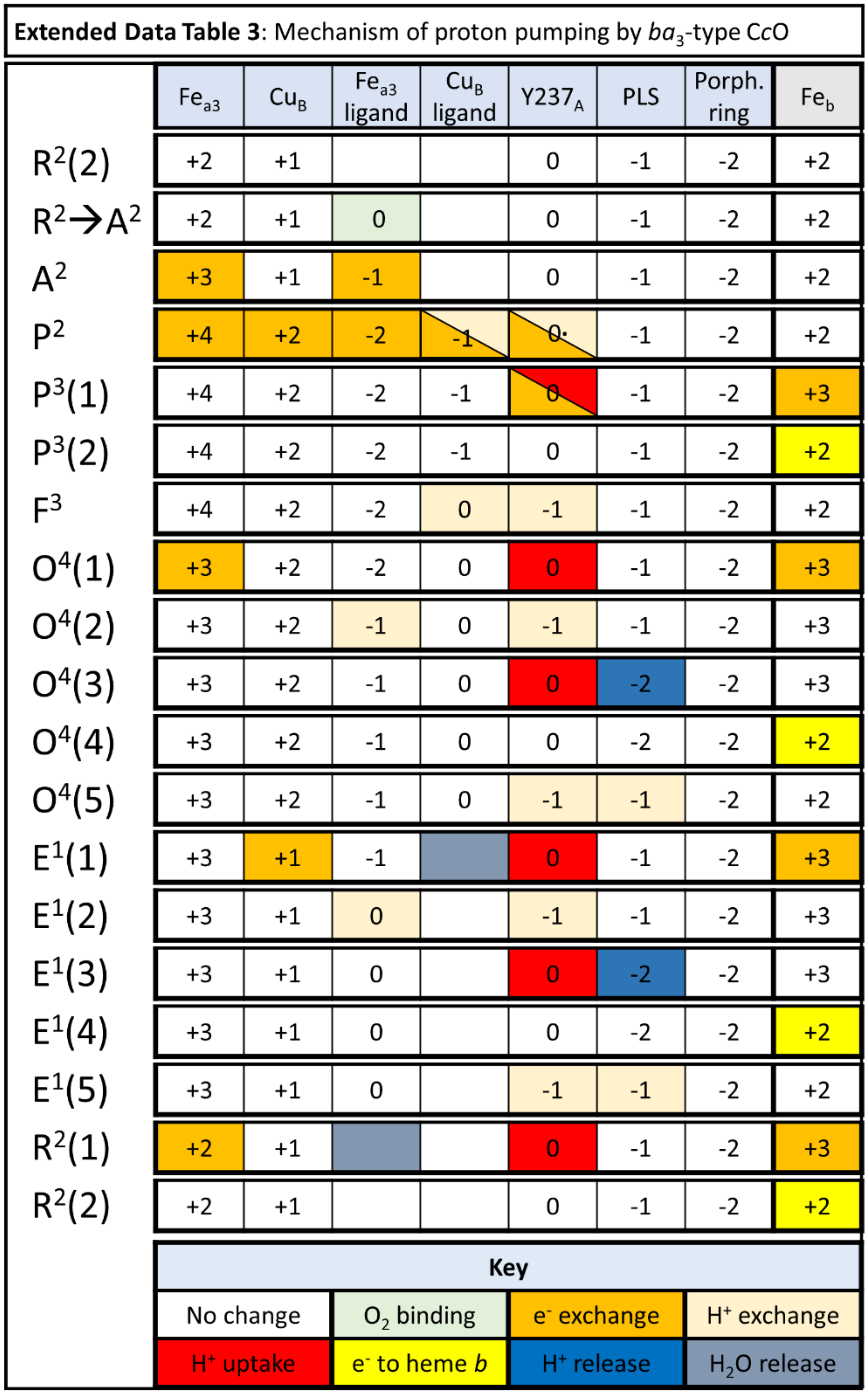

	Fe$_{a3}$	Cu$_B$	Fe$_{a3}$ ligand	Cu$_B$ ligand	Y237$_A$	PLS	Porph. ring	Fe$_b$
R^2(2)	+2	+1			0	-1	-2	+2
R^2→A^2	+2	+1	0		0	-1	-2	+2
A^2	+3	+1	-1		0	-1	-2	+2
P^2	+4	+2	-2	-1	0·	-1	-2	+2
P^3(1)	+4	+2	-2	-1	0	-1	-2	+3
P^3(2)	+4	+2	-2	-1	0	-1	-2	+2
F^3	+4	+2	-2	0	-1	-1	-2	+2
O^4(1)	+3	+2	-2	0	0	-1	-2	+3
O^4(2)	+3	+2	-1	0	-1	-1	-2	+3
O^4(3)	+3	+2	-1	0	0	-2	-2	+3
O^4(4)	+3	+2	-1	0	0	-2	-2	+2
O^4(5)	+3	+2	-1	0	-1	-1	-2	+2
E^1(1)	+3	+1	-1		0	-1	-2	+3
E^1(2)	+3	+1	0		-1	-1	-2	+3
E^1(3)	+3	+1	0		0	-2	-2	+3
E^1(4)	+3	+1	0		0	-2	-2	+2
E^1(5)	+3	+1	0		-1	-1	-2	+2
R^2(1)	+2	+1			0	-1	-2	+3
R^2(2)	+2	+1			0	-1	-2	+2

Key			
No change	O$_2$ binding	e$^-$ exchange	H$^+$ exchange
H$^+$ uptake	e$^-$ to heme *b*	H$^+$ release	H$_2$O release

Captions to Supplementary Videos

Supplementary Video 1: Electron density observed at the BNC of *ba*$_3$-C*c*O under different redox conditions. This video rotates the electron density maps shown in **Fig. 2** through 360°.

Supplementary Video 2: Electron density changes observed within the BNC of *ba*$_3$-C*c*O induced by the release of photocaged oxygen by a UV laser pulse. This video rotates the electron density maps shown in **Fig. 3** through 360°.

Supplementary Video 3: Atomistic mechanism of proton pumping by the *ba*$_3$-type C*c*O. This schematic represents how chemical changes within the BNC as dioxygen is reduced to two water molecules, are coupled to the pumping of two protons by the *ba*$_3$-type C*c*O. To preserve the principle of electroneutrality, the active-site charges associated with the iron atom of haem *a*$_3$, the porphyrin ring of haem *a*$_3$, the copper atom of Cu$_B$, the oxygen species ligating haem *a*$_3$ or Cu$_B$, the charge of Tyr237, and the charge of the PLS, are required sum to zero for every step of this reaction. The charge of the iron atom of haem *b*, which controls the pKa of the PLS, is also represented. This schematic is drawn to emphasize how protons are transported along a chain of water molecules and protonatable groups *via* Grotthuss' mechanism. Every step of this mechanism is summarized in **Extended Data Table 3**. For every reaction turnover, four electrons enter the active site *via* haem *b*, six protons are taken up to Tyr237 from the *N*-side of the membrane, and two protons are released by the PLS to the *P*-side of the membrane.

SUPPLEMENTARY REFERENCES

47 Andersson, R. *et al.* Well-based crystallization of lipidic cubic phase microcrystals for serial X-ray crystallography experiments. *Acta Crystallogr D Struct Biol* **75**, 937-946 (2019). https://doi.org/10.1107/S2059798319012695

48 Chen, Y., Hunsicker-Wang, L., Pacoma, R. L., Luna, E. & Fee, J. A. A homologous expression system for obtaining engineered cytochrome ba_3 from Thermus thermophilus HB8. *Protein Expr Purif* **40**, 299-318 (2005). https://doi.org/10.1016/j.pep.2004.11.014

49 Caffrey, M. & Porter, C. Crystallizing membrane proteins for structure determination using lipidic mesophases. *J Vis Exp* (2010). https://doi.org/10.3791/1712

50 Ludovici, C., Frohlich, R., Vogtt, K., Mamat, B. & Lubben, M. Caged O_2. Reaction of cytochrome bo_3 oxidase with photochemically released dioxygen from a cobalt peroxo complex. *Eur J Biochem* **269**, 2630-2637 (2002). https://doi.org/10.1046/j.1432-1033.2002.02944.x

51 Lukesh, J. C., 3rd, Palte, M. J. & Raines, R. T. A potent, versatile disulfide-reducing agent from aspartic acid. *J Am Chem Soc* **134**, 4057-4059 (2012). https://doi.org/10.1021/ja211931f

52 Schmidt, M. Mix and Inject: Reaction Initiation by Diffusion for Time-Resolved Macromolecular Crystallography. *Adv. Cond. Mat. Phys.* , 167276 (2013).

53 Hadfield, A. & Hajdu, J. A fast and portable microspectrophotometer for protein crystallography. *J. Appl. Cryst.* **26**, 839-842 (1993).

54 Ghosh, S. *et al.* A simple goniometer-compatible flow cell for serial synchrotron X-ray crystallography. *J. Appl. Crytallogr.* **56** (2023).

55 White, T. a. *et al.* CrystFEL : a software suite for snapshot serial crystallography. *Journal of Applied Crystallography* **45**, 335-341 (2012). https://doi.org/10.1107/S0021889812002312

56 White, T. A. *et al.* Recent developments in CrystFEL. *J Appl Crystallogr* **49**, 680-689 (2016). https://doi.org/10.1107/S1600576716004751

57 Winn, M. D. *et al.* Overview of the CCP4 suite and current developments. *Acta Crystallogr D Biol Crystallogr* **67**, 235-242 (2011). https://doi.org/10.1107/S0907444910045749

58 McCoy, A. J. *et al.* Phaser crystallographic software. *J Appl Crystallogr* **40**, 658-674 (2007). https://doi.org/10.1107/S0021889807021206

59 Emsley, P. & Cowtan, K. Coot: model-building tools for molecular graphics. *Acta Crystallogr D Biol Crystallogr* **60**, 2126-2132 (2004). https://doi.org/10.1107/S0907444904019158

60 The PyMOL Molecular Graphics System v. Version 1.2r3pre (Schrödinger, LLC.).

61 Vallejos, A., Katona, G. & Neutze, R. Appraising protein conformational changes by resampling time-resolved serial X-ray crystallography data. *Struct. Dyn.* (2024).

62 Coquelle, N. *et al.* Chromophore twisting in the excited state of a photoswitchable fluorescent protein captured by time-resolved serial femtosecond crystallography. *Nat Chem* **10**, 31-37 (2018). https://doi.org/10.1038/nchem.2853

63 Liebschner, D. *et al.* Polder maps: improving OMIT maps by excluding bulk solvent. *Acta Crystallogr D Struct Biol* **73**, 148-157 (2017). https://doi.org/10.1107/S2059798316018210

64 Wickstrand, C. *et al.* A tool for visualizing protein motions in time-resolved crystallography. *Struct. Dyn.* **7**, 024701 (2020). https://doi.org/doi: 10.1063/1.5126921

65 Henderson, R. & Moffat, J. K. The difference Fourier technique in protein crystallography: errors and their treatment. *Acta Crystallogr. B* **27**, 1414-1420 (1971).

66 Liu, J., Qin, L. & Ferguson-Miller, S. Crystallographic and online spectral evidence for role of conformational change and conserved water in cytochrome oxidase proton pump. *Proc Natl Acad Sci U S A* **108**, 1284-1289 (2011). https://doi.org/10.1073/pnas.1012846108

67 Ishigami, I. *et al.* Crystal structure of CO-bound cytochrome c oxidase determined by serial femtosecond X-ray crystallography at room temperature. *Proc Natl Acad Sci U S A* **114**, 8011-8016 (2017). https://doi.org/10.1073/pnas.1705628114